Inorganic Chemistry

Article

pubs.acs.org/IC

Tuning Sodium Ion Conductivity in the Layered Honeycomb Oxide $Na_{3-x}Sn_{2-x}Sb_xNaO_6$

Rebecca W. Smaha,*[†,∥] John H. Roudebush,[†] Jake T. Herb,[†,‡] Elizabeth M. Seibel,[†] Jason W. Krizan,[†] Gary M. Fox,[†] Qingzhen Huang,[§] Craig B. Arnold,[‡] and Robert J. Cava[†]

[†]Department of Chemistry, [‡]Department of Mechanical and Aerospace Engineering, Princeton University, Princeton, New Jersey 08544, United States

[§]NIST Center for Neutron Research, Gaithersburg, Maryland 20899-6102, United States

Supporting Information

ABSTRACT: A series of compounds with the composition $Na_{3-x}Sn_{2-x}Sb_xNaO_6$ (x = 0.0, 0.2, 0.4, 0.6, 0.7, 0.8, 0.9, and 1.0) has been prepared by solid-state reaction and characterized by powder X-ray diffraction, neutron diffraction (for x = 0.0), and impedance spectroscopy. The compounds have a layered structure derived from that of α-$NaFeO_2$, with alternating Na_3 planes and $NaSn_2O_6$ slabs with honeycomb in-plane ordering. The structure of the parent compound, Na_2SnO_3, has been determined as a two-layer honeycomb in monoclinic space group $C2/c$. Due to charge neutrality requirements, the substitution of Sb^{5+} for Sn^{4+} creates sodium site vacancies that facilitate high sodium ion mobility. A decrease in layer stacking disorder is also observed. The conductivity increases linearly with x and has a maximum at x = 0.8 (1.43×10^{-3} S/cm at 500 °C with suboptimal sample densities). This material may be of interest as a solid Na ion electrolyte.

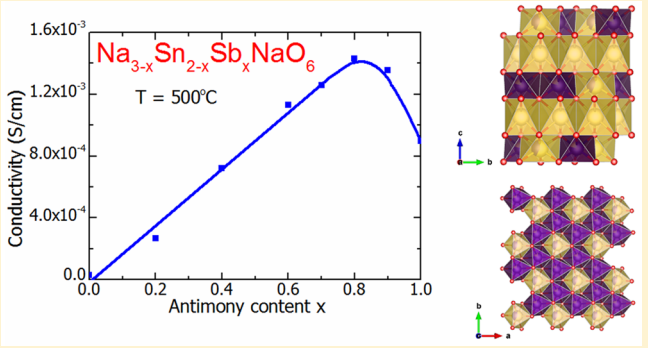

1. INTRODUCTION

Layered compounds are integral to current battery technologies, especially as cathodes in Li- or Na-ion batteries.[1−3] Li_xCoO_2 and Na_xCoO_2, for example, are among the most commonly studied cathode materials due to their stability and ease of Li or Na insertion and removal.[4,5] Materials that conduct ions but are electronically insulating can be used as solid-state electrolytes, which are intrinsically safer than liquid electrolytes, but their use has been hindered by the relatively low ionic conductivity of known materials and their subsequently higher required operating temperatures.[1,6] Many layered compounds act as ion conductors, with temperature being the most important factor affecting conductivity. For instance, the alkali cations in Li_2SnO_3 and α-$NaFeO_2$ are somewhat mobile.[7,8] Na-ion battery materials have been less studied than their lithium analogues but have potential due to the lower materials cost of Na compared to Li.[6,9] Some Na-ion conducting materials have been investigated as possible solid-phase electrolytes, including β-alumina[6,10] and NASICON, a family of zirconia-based Na superionic conductors whose structure allows for the movement of Na ions through 3D channels at elevated temperatures, leading to high ionic conductivity.[11−13]

The current study is based on materials related to the α-$NaFeO_2$ structure type, generically represented as ABO_2 compounds, which consist of layers of A^{1+} cations and layers of B^{3+} cations forming close-packed BO_2 layers of edge-sharing BO_6 octahedra.[14,15] The layers of BO_6 octahedra may be stacked in several ways, which commonly creates 3R-like (e.g., T1 and O3) or 2H-like (e.g., P2 and P3) polytypes.[16] With multiple B-site cations, an ordered honeycomb variant of the structure can be formed with the general formula $A_3B'_2B''O_6$. The long-range ordering of the B′ and B″ ions in the honeycomb results in an expanded basal plane compared to α-$NaFeO_2$. These structures are often described in a monoclinic space group[14,17] due to a deviation in the stacking of the layers from perfect orthogonality, giving rise to additional stacking options such as O1 and O2.[17]

Recently, two sets of honeycomb derivatives of the $NaFeO_2$ structure were prepared that showed high Na ion conductivity: $Na_2M_2TeO_6$ (M = Ni, Co, Zn, Mg) and $Na_x(M_yL_{1-y})O_2$ (M = Ni, Fe; L = Ti, Sb).[18,19] However, the fraction of filled sites in the Na layers was not optimized in these studies. Here, this optimization is accomplished through partial substitution of Sb^{5+} for Sn^{4+} in the parent compound Na_2SnO_3, yielding compounds of the type $Na_{3-x}Sn_{2-x}Sb_xNaO_6$. This substitution, based on oxidation states and similar atomic sizes, is a simple way to create phases with deficient Na layers. The family of Na-containing layered honeycomb compounds is large; thus, an investigation of the ionic conductivity of new materials within

Received: May 26, 2015
Published: July 27, 2015

DOI: 10.1021/acs.inorgchem.5b01186
Inorg. Chem. 2015, 54, 7985−7991

this group may provide valuable insight into the nature of conductivity and elucidate new solid-state electrolytes.

2. EXPERIMENTAL SECTION

Samples with the composition $Na_{3-x}Sn_{2-x}Sb_xNaO_6$ (x = 0.0, 0.2, 0.4, 0.6, 0.7, 0.8, 0.9, and 1.0) were synthesized by standard solid-state methods. Stoichiometric amounts of dry Na_2CO_3 (Alfa Aesar 99.5%), SnO_2 (Alfa Aesar 99.9%), and Sb_2O_5 (Alfa Aesar 99.998%) were ground together. The sample with x = 0 (Na_2SnO_3) destined for neutron diffraction was made by heating the pelletized precursors at 800 °C for 12 h, cooling to 650 °C, and then quenching the pellet directly into the glovebox. This sample will be denoted Na_2SnO_3-LT (low temperature). On the other hand, the samples ($0 \leq x \leq 1$) destined for eventual electrochemical measurements, denoted HT (high temperature) samples, were prereacted as loose powder at 750 °C for 18 h followed by regrinding and filtering through a 140 μm sieve. Next, these samples were pelletized and sintered at 1300 °C for 6 h and quenched in air while buried in a prereacted powder of nominal composition $Na_4Sn_3O_8$ in order to avoid Na or Sb vaporization. $Na_4Sn_3O_8$ was chosen because it is stable at higher temperatures than Na_2SnO_3 is and because its Na/Sn ratio is greater than 1:1, as is desired for the $Na_{3-x}Sn_{2-x}Sb_xNaO_6$ samples.[20,21]

Phase purity was determined by powder X-ray diffraction (PXRD) performed on a Bruker D8 Advance ECO diffractometer and a Bruker D8 Focus diffractometer with Cu Kα radiation. A neutron powder diffraction (NPD) pattern for Na_2SnO_3-LT was collected at 300 K on the BT-1 diffractometer at the NIST Center for Neutron Research using a Cu(311) monochromator with wavelength 1.5403 Å. Data was collected over the range of 3−167.75° 2θ with a step size of 0.05°. The FullProf software suite was used to perform Rietveld structure refinements for Na_2SnO_3-LT, modeling peak shapes with the Thompson−Cox−Hastings pseudo-Voight profile convoluted with axial divergence asymmetry.[22] A corefinement of PXRD and NPD data was performed for Na_2SnO_3-LT over the data range 5−110° 2θ for PXRD and 3−150° 2θ for NPD. LeBail profile fits were performed on PXRD patterns of HT samples with $x > 0$.

Ionic conductivity measurements were performed to analyze the system's electrochemical properties. To increase final pellet density, stearic acid ($CH_3(CH_2)_{16}CO_2H$, Fisher Scientific reagent grade) was added to each HT sample in a 16:1 molar ratio and dissolved with ethanol. The resulting mixture was dried, reground, and pressed into a 0.5 in. diameter pellet. Buried pellets were sintered at 1000 °C for 4 h in air and quenched. Initial PXRD tests on ground powder of the resulting pellets confirmed that this method of pellet densification conserves the phase purity. Impedance spectroscopy was performed on these pellets using a Solartron Analytical 1260 frequency analyzer coupled with a Solartron Analytical 1287 electrochemical interface. The impedance analyzer was connected to a purpose-built device that allows for tests to be taken at a range of temperatures under flowing argon. Because silver and sodium have similar atomic sizes and the same charge, gold paint was employed as blocking electrodes. After baking the system at 500 °C overnight under argon flow to eliminate adventitious water, impedance scans were taken every 50 °C from 500 to 200 °C over the frequency range of 100 000 to 0.01 Hz at an AC amplitude of 10 mV. The sample resistance was taken as the extrapolation of the electrode impedance to the real impedance axis in the Nyquist plots.

3. RESULTS AND DISCUSSION

3.1. Structure. *3.1.1. Structure of Na_2SnO_3.* Na_2SnO_3 has been previously been reported in space group $R\bar{3}m$ (No. 166),[21] although this space group does not capture the honeycomb ordering, which requires an expansion of the basal plane (see Figure 1). This order produces sharp supercell reflections in the 2θ range 18−30° (Cu Kα) that are not fully indexed by the space group $R\bar{3}m$ because this symmetry implies full Na/Sn disorder and thus a lack of supercell reflections. Using a monoclinic unit cell allows for the fully ordered

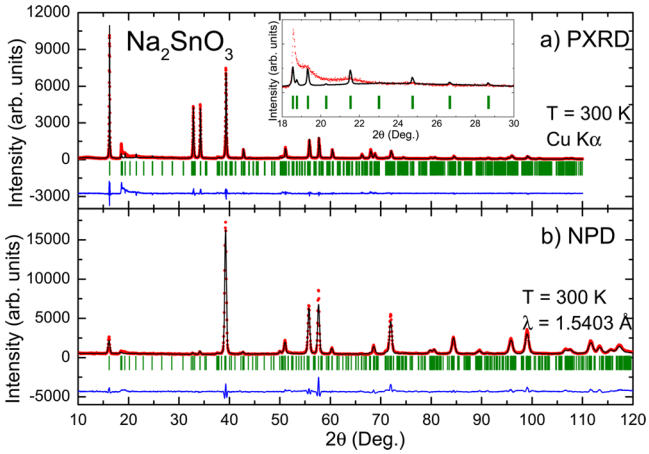

Figure 1. (a) PXRD and (b) NPD patterns of Na_2SnO_3 taken at room temperature, including Rietveld refinements in monoclinic space group $C2/c$ (No. 15). Observed (red), calculated (black), and difference (blue) plots are shown, and Bragg reflections are indicated by green tick marks. The inset in (a) magnifies the coloring fault region (18−30° 2θ).

honeycomb to be described, accounting for the observed supercell reflections. Therefore, the structure of parent compound Na_2SnO_3 has been determined in space group $C2/c$ (No. 15) and is depicted in Figure 2,[23] showing its layered

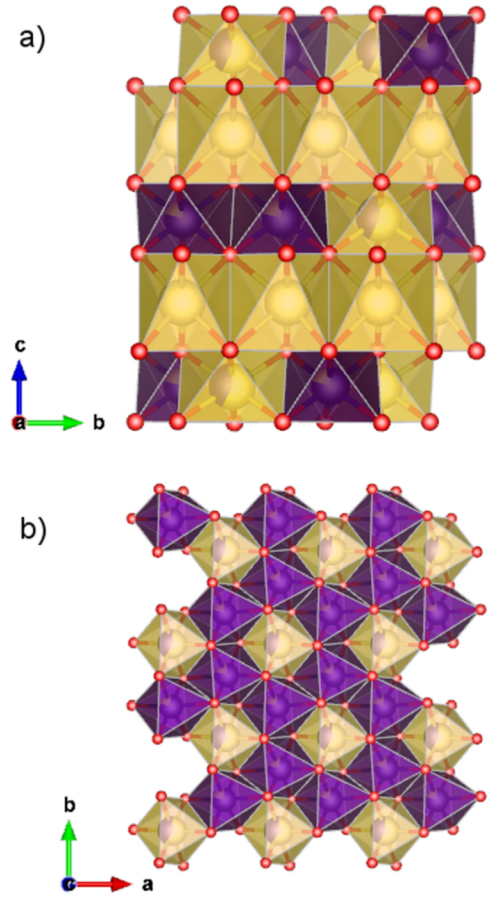

Figure 2. Structure of Na_2SnO_3 in space group $C2/c$ (No. 15). (a) View along a-axis; (b) view of the Sn/Na honeycomb layer. Na atoms are yellow, Sn atoms are purple, and O atoms are red.

DOI: 10.1021/acs.inorgchem.5b01186
Inorg. Chem. 2015, 54, 7985−7991

Table 1. Crystallographic Data for Na_2SnO_3 in Monoclinic Space Group $C2/c$ (No. 15) Elucidated through Corefinement of PXRD and NPD Data[a]

site	atom	Wyckoff position	x	y	z	B_{iso}	occ.
A	Na(1)	4e	0.5	0.579(3)	0.25	2.5(1)	1
A	Na(2)	4e	0	0.439(3)	0.25	2.5(1)	1
A	Na(3)	4e	0	0.75	0.25	2.5(1)	1
B′	Sn(1)	8f	0.2639(9)	0.0836(4)	0.0007(8)	1.85(5)	0.212(3)
B′	Na(4)	8f	0.2639(9)	0.0836(4)	0.0007(8)	1.85(5)	0.788(3)
B″	Na(5)	4d	0.75	0.25	0	1.85(5)	0.575(3)
B″	Sn(2)	4d	0.75	0.25	0	1.85(5)	0.425(3)
O	O(1)	8f	0.388(2)	0.257(1)	0.8917(8)	0.83(3)	1
O	O(2)	8f	0.628(2)	0.079(1)	0.106(1)	0.83(3)	1
O	O(3)	8f	0.647(2)	0.435(1)	0.104(1)	0.83(3)	1

[a] a = 5.5274(1) Å, b = 9.5746(3) Å, c = 11.0831(2) Å, β = 99.689(2)°, V = 578.17 Å^3. For the PXRD pattern: χ^2 = 7.10, wR_p = 18.8, R_p = 12.5, $R(F^2)$ = 7.06. For the NPD pattern: χ^2 = 7.18, wR_p = 9.75, R_p = 7.75, $R(F^2)$ = 3.64. The apparent mixed occupancy of the B′ and B″ sites is a reflection of the presence of stacking faults, not in-plane disorder.

nature and an ordered honeycomb of Sn atoms around a central Na in the Na−Sn layer. The honeycomb pattern is evident on looking down on the a−b plane: in this layer, the B′ sites (Sn) form honeycombs around octahedral B″ sites (Na). Therefore, an expanded formula could be be written as $Na_3Sn_2NaO_6$ to emphasize the honeycomb ordering. Although this compound is 3R-like, we adopt the notation O2 to describe the monoclinic setting.

The analogous structure Na_2IrO_3 has also been reported in $C2/c$ with double the c-axis (i.e., as a two-layer cell).[24,25] The distinction between $C2/m$ (No. 12) and $C2/c$ unit cells for honeycomb materials is a topic of ongoing research;[26] Na_2IrO_3, for example, has been reported in both $C2/c$[24] and $C2/m$.[27] We chose $C2/c$ for the current material because as Sb content x increases, the expected superlattice peaks match a $C2/c$ unit cell, as will be discussed further below. Figure 1 and Table 1 show the results of corefining PXRD and NPD patterns in space group $C2/c$. Selected bond lengths are shown in Table 2.

Table 2. Selected Na_2SnO_3 Bond Distances (Å)

atoms	distance (Å)
Na(1)−O(1) × 2	2.37(3)
Na(1)−O(2) × 2	2.38(1)
Na(1)−O(3) × 2	2.37(3)
Na(2)−O(1) × 2	2.59(3)
Na(2)−O(2) × 2	2.29(3)
Na(2)−O(3) × 2	2.31(1)
Na(3)−O(1) × 2	2.437(9)
Na(3)−O(2) × 2	2.48(1)
Na(3)−O(3) × 2	2.62(1)
Sn(1)−O(1)	2.23(1) and 2.19(1)
Sn(1)−O(2)	2.10(2) and 2.15(1)
Sn(1)−O(3)	2.38(1) and 2.01(1)
Na(5)−O(1) × 2	2.154(9)
Na(5)−O(2) × 2	2.19(1)
Na(5)−O(3) × 2	2.24(1)

Irregular stacking of the honeycomb layers is known to occur in these types of materials.[14,28] In the α-$NaFeO_2$ structure, stacking faults are common; they manifest as Warren line shapes.[29] In layered honeycomb materials, further consideration should be given to the distinction of the B′ and B″ ions, a phenomenon that has been called coloring faults.[28] The Warren line shape is seen in the current materials in the diffraction angle range of 18−24° (Cu Kα) (see, for example, the inset to Figure 1). Therefore, the refinement of this O2 two-layer monoclinic honeycomb was performed analogously to previous Na-containing honeycombs,[14,30] which allows for Na/Sn site mixing to account for stacking and coloring faults. The mixed occupancy observed on the B′ and B″ sites equates to approximately 21% faulting.

3.1.2. Antimony-Substituted $Na_{3-x}Sn_{2-x}Sb_xNaO_6$. The Sb-substituted compounds with nominal composition $Na_{3-x}Sn_{2-x}Sb_xNaO_6$, $0 \le x \le 1$, were successfully synthesized using standard solid-state techniques. An O2 layered structure, analogous to that of the parent compound, was found to be stable for all compositions. Examining the diffraction data of the x = 0.9 and 1.0 samples (Figure 3), new reflections can be observed, including a peak at ∼15°, near the largest peak of the O2 phase (marked in Figure 3b). This new peak suggests the presence of a second polytype. The new peaks can be successfully indexed to a two-layer hexagonal unit cell, and marking the emergence of a 2H-like polytype of $Na_{3-x}Sn_{2-x}Sb_xNaO_6$. Figure 3a shows the PXRD patterns of the samples synthesized in this series; the two largest peaks corresponding to small amounts of the second polytype are marked with asterisks for x > 0.8. Further work is required to isolate the observed 2H-like phase and better determine its structure.

Due to the indistinguishability of Sn and Sb in XRD and to the presence of a second phase at higher values of x, it was not possible to perform Rietveld refinements on this data. Coincident peaks create uncertainty in the refined values of the B′ and B″ site occupancies and the atomic positions. Future work on site occupancies is warranted to elucidate the nature of Sb substitution and its effects on Na occupancy. Thus, LeBail profile fits of the PXRD patterns were performed in the monoclinic space group $C2/c$ (No. 15) for x > 0. For samples with x > 0.8, the 2H-like phase was included in the fit using space group $P6_3/mmc$ (No. 194), typical of 2H variants.[28] Representative plots of these fits for x = 0.8 and 0.9 are graphed in Figure 4. As these examples show, the inclusion of both polytypes gave good fits to the observed patterns, successfully indexing all supercell peaks in the 18−24° 2θ region (seen in Figure 3b and in the insets of Figure 4). This confirms that $C2/c$ is the appropriate choice of space group for this phase and thus for the parent compound, Na_2SnO_3, as well.

The increase in the c-axis lattice parameter can be seen directly in the PXRD patterns: for x = 0.0, there are two

DOI: 10.1021/acs.inorgchem.5b01186
Inorg. Chem. 2015, 54, 7985−7991

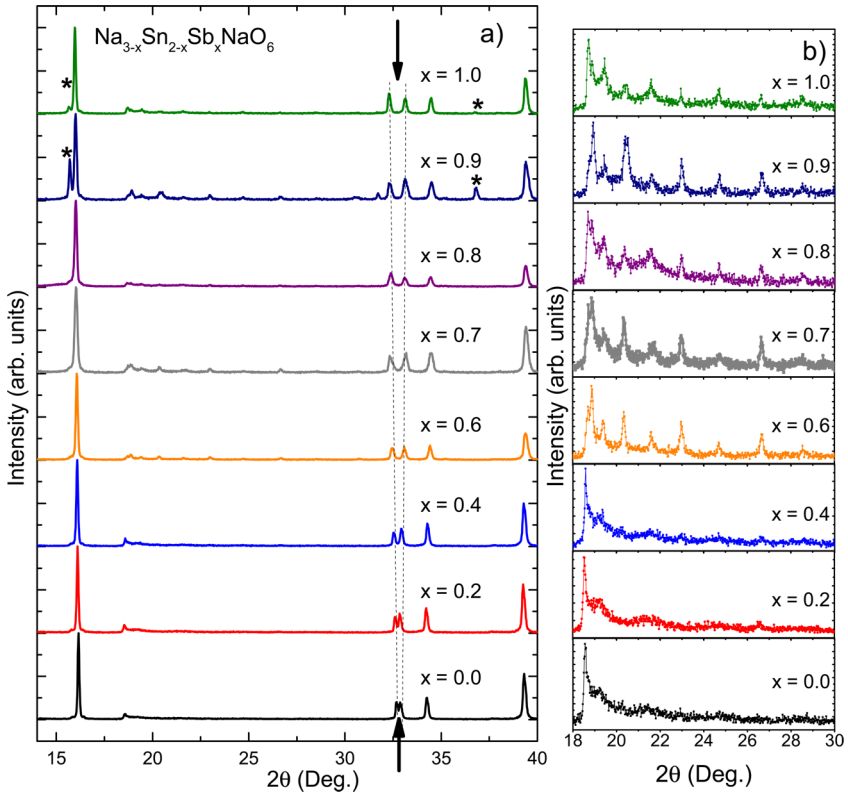

Figure 3. (a) Powder X-ray diffraction patterns of $Na_{3-x}Sn_{2-x}Sb_xNaO_6$, $0 \leq x \leq 1$. Peaks at $2\theta = 32.5°$ corresponding to Bragg reflections (004) and (200)/(−131) are marked with arrows and dashed lines. The two largest peaks corresponding to a 2H-like polytype are marked with asterisks for $x \geq 0.9$. (b) Powder X-ray diffraction patterns for the coloring fault region (18−30° 2θ).

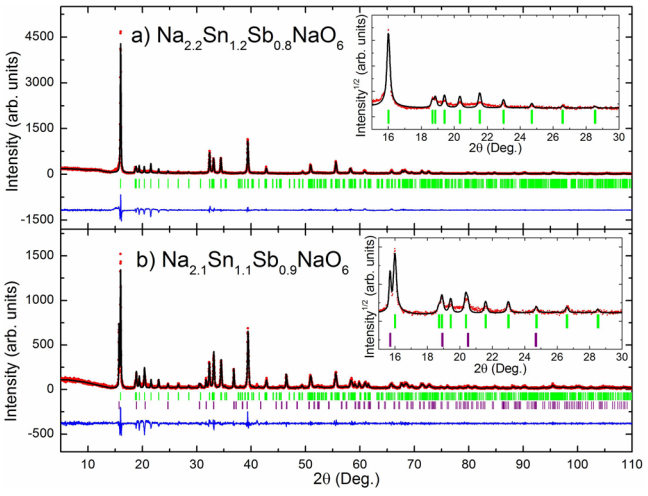

Figure 4. (a) PXRD pattern taken at room temperature and LeBail profile fit of $Na_{2.2}Sn_{1.2}Sb_{0.8}NaO_6$. The green tick marks correspond to Bragg reflections of monoclinic space group $C2/c$ (No. 15). (b) PXRD pattern taken at room temperature and LeBail profile fit of $Na_{2.1}Sn_{1.1}Sb_{0.9}NaO_6$. The green tick marks correspond to Bragg reflections of monoclinic space group $C2/c$, and the purple tick marks correspond to Bragg reflections of the 2H-like polytype in space group $P6_3/mmc$ (No. 194). The insets in (a) and (b) magnify the coloring fault region (15−30° 2θ) using the square root of intensity values.

coincident peaks at $2\theta = \sim 32.5°$ that move apart as Sb content increases (marked with arrows in Figure 3a). They are marked with arrows in Figure 3a. The left-hand peak corresponds to the (004) Bragg reflection; as c increases, this peak shifts to the left and creates the observed trend in peak separation. The right-hand peak corresponds to the (200) and (−131) reflections and moves slightly to the right due to the decrease in a and b.

The lattice parameters and layer spacing d_{001} for the series are listed in Table 3 and graphed in Figure 5. Lattice parameters for the 2H-like polytype are noted in the caption of Table 3. The layer spacing d_{LS} was calculated by using $d_{LS} = (^1/_2)c_{monoclinic}\cos(\beta - 90°)$.[31] As Sb content x increases, the in-plane lattice parameter a decreases, confirming the introduction of Sb into the compound given the smaller radius of Sb^{5+} than Sn^{4+}. Simultaneously, c and the layer spacing increase, as is expected due to the weakening of the intralayer bonding though the removal of some Na from the Na layers. The introduced Sb can reasonably be expected to occupy the honeycomb layer, given its similarity to Sn in terms of both ionic radius and charge as compared to those of Na, which is consistent with the lattice parameter trend that suggests a shrinking of the honeycomb layer. Compounds such as $Na_3M_2SbO_6$ (M = Cu, Ni, Co, Mg, Zn) with Sb occupying the metal octahedra slabs show that this is a viable model.[32−34] Although structure refinements of the Sb-substituted samples are not reported due to the inability to distinguish Sn and Sb in XRD, initial Rietveld refinements indicate that the Na sites between the honeycomb layers are deficient. It is well-known that the alkali sites between the metal-oxide layers are mobile, as evidenced by deintercalation and ion-exchange reactions of α-$NaFeO_2$-type compounds like Na_xCoO_2, Li_xCoO_2, $Li_3Ni_2BiO_6$, $Na_3Ni_2SbO_6$, and $Na_3Ni_2BiO_6$.[4,5,30,35−38]

As the Sb content increases, the Warren line shapes that arise in the 2θ range 18−30° due to the stacking faults in the parent material decrease in intensity. In their place, more conventional superlattice peaks matching space group $C2/c$ become sharper

DOI: 10.1021/acs.inorgchem.5b01186
Inorg. Chem. 2015, 54, 7985−7991

Table 3. Lattice Parameters and Layer Spacing of $Na_{3-x}Sn_{2-x}Sb_xNaO_6$, $0 \le x \le 1$, Extracted from the Rietveld Refinement of Na_2SnO_3 and from LeBail Profile Fits of PXRD Data for $x > 0$ in Space Group $C2/c$ (No. 15)[a]

Sb content (x)	a (Å)	b (Å)	c (Å)	β (deg.)	layer spacing (Å)
0.0	5.5274(1)	9.5746(3)	11.0831(2)	99.689(2)	5.3492(6)
0.2	5.5166(2)	9.5508(4)	11.1155(4)	99.543(3)	5.5190(4)
0.4	5.5071(2)	9.5327(5)	11.1469(4)	99.521(3)	5.5477(3)
0.6	5.4849(2)	9.4998(4)	11.1842(4)	99.567(3)	5.5356(5)
0.7	5.4784(3)	9.4804(4)	11.2144(5)	99.551(4)	5.5626(6)
0.8	5.4833(3)	9.4836(5)	11.2014(4)	99.484(4)	5.5909(3)
0.9	5.4806(3)	9.4792(5)	11.2315(5)	99.572(5)	5.5550(8)
1.0	5.4816(2)	9.4769(3)	11.2260(4)	99.475(3)	5.6059(2)

[a]For $x \ge 0.9$, the 2H-like polytype was included in the profile fit with lattice parameters a = 5.4140(3) Å and c = 11.2808(6) Å for x = 0.9 and a = 5.4087(5) Å and c = 11.292(1) Å for x = 1.0.

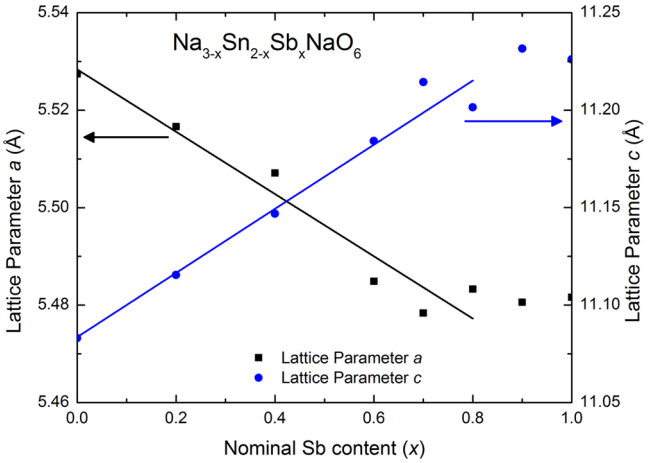

Figure 5. Lattice parameters extracted from LeBail profile fits of $Na_{3-x}Sn_{2-x}Sb_xNaO_6$ using space group $C2/c$ (No. 15) as a function of nominal Sb content x. Error bars are smaller than the symbols, and lines are linear fits to the data for the single-phase solid solution, $0 \le x \le 0.8$.

and better defined, as evident in Figure 3b. The sharpening of the ordering peaks with increasing Sb content confirms that the stacking faults decrease in fraction as the Sb content increases, reflecting a higher degree of order in the structure.

Mobile alkali cations in layered materials, like the Na atoms found between the honeycomb sheets, can often have interesting electrochemical behavior. Therefore, we set out to measure the mobility of these Na ions as a function of Sb doping

3.2. Sodium Ion Conductivity. The Na ionic conductivity of $Na_{3-x}Sn_{2-x}Sb_xNaO_6$ was tested using electrochemical impedance spectroscopy (EIS) over a range of temperatures. The highest sample densities achieved in this work (see Table 4) are approximately 65%. Measured ionic conductivity values depend on the density of the sample; the densities obtained in this work were low, and higher conductivity values are expected for denser samples, likely by a factor of approximately 2.[26,39]

Figure 6 shows representative Nyquist plots of $Na_{2.2}Sn_{1.2}Sb_{0.8}NaO_6$ over the temperature range 315−475 °C. They demonstrate the expected behavior of an ion conductor: a semicircle arising from the sample's capacitance and resistance and a straight line that is a product of the Warburg effect. For samples measured at T > 315 °C, induction effects are also present in the measurement circuit, leading to distorted semicircles.

Table 4. Densities, Activation Energies, and Ionic Conductivities at 500 °C for $Na_{3-x}Sn_{2-x}Sb_xNaO_6$, $0 \le x \le 1$[a]

Sb content (x)	density (%)	activation energy (eV)	conductivity at 500 °C (S/cm)
0.0	63.8	0.78	2.92×10^{-5}
0.2	66.3	0.70	2.69×10^{-4}
0.4	69.1	0.62	7.21×10^{-4}
0.6	64.0	0.65	1.13×10^{-3}
0.7	67.9	0.68	1.26×10^{-3}
0.8	68.3	0.63	1.43×10^{-3}
0.9	69.3	0.62	1.36×10^{-3}
1.0	62.9	0.58	8.96×10^{-4}

[a]Densities are given as a percent of theoretical. Activation energies were calculated using the Arrhenius equation from 473 to 773 K. Impurities of the 2H-like polytype are seen in the samples with x > 0.8.

For all samples, ionic conductivity increased with increasing temperature, and the highest conductivity values were found at 500 °C, the highest temperature measured. Figure 7 shows the conductivity values at 500 °C as a function of the Sb content (x) of each sample (Table 4). Error bars are not included due to difficulty in calculating the combined error from area measurements, device inductance, and the impedance frequency analyzer. There is a linear increase in the conductivity as a function of Sb content until x = 0.8, after which there is a decrease. Figure 8 plots the logarithm of ionic conductivity versus inverse temperature; the trends are consistent with those in Figure 7. The behavior is linear, as expected given that ionic conductivity is a diffusion (and therefore activated and temperature-dependent) process.

The conductivity activation energies (E_a) for each compound were calculated with the Arrhenius equation

$$\sigma = \frac{\sigma_0}{T} \exp(-E_a/kT)$$

using linear fits of the slopes of the plots in Figure 8. The figure shows that the conductivity data are well-described by the Arrhenius relationship. The activation energies decrease systematically as a function of Na ion concentration (see Table 4). This decrease in activation energy with increasing vacancy concentration could be a reflection of an increased size of the diffusion bottleneck that arises as a consequence of the expansion of the c-axis (and thus the Na layer height) when the c-axis expands as a function of increasing Sb content. After the initial decrease in conductivity activation energy on introduction of vacant Na sites, the variation is relatively small for the remainder of the series, with the changes in conductivity attributable to a larger fraction of available vacant sodium sites.

DOI: 10.1021/acs.inorgchem.5b01186
Inorg. Chem. 2015, 54, 7985−7991

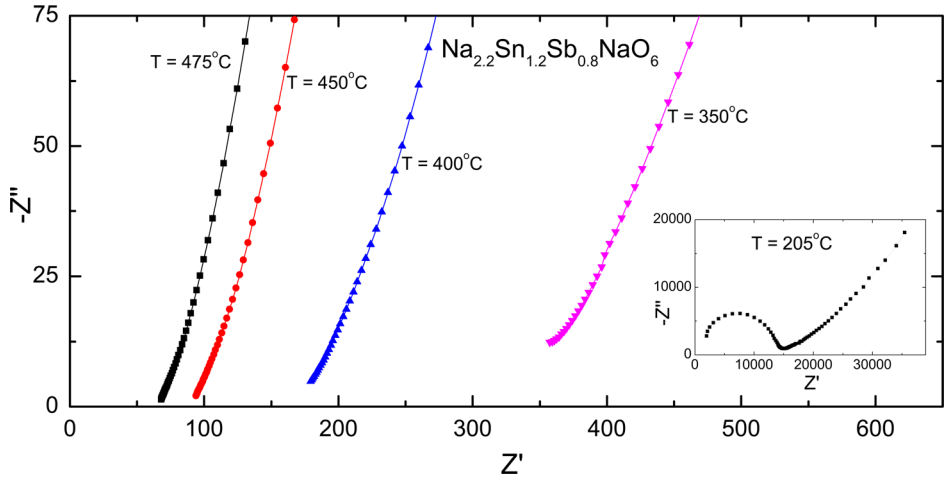

Figure 6. Representative Nyquist plots for $Na_{2.2}Sn_{1.2}Sb_{0.8}NaO_6$ from 350 to 475 °C measured at frequencies less than 100 000 Hz. Positive values of Z'' at high temperatures (not shown here) are due to circuit inductive effects. The inset shows the semicircular behavior of the plot for 205 °C measured at frequencies less than 1 000 000 Hz.

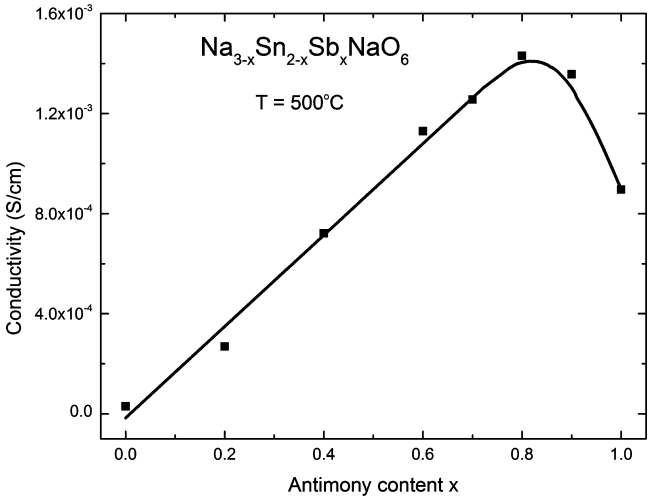

Figure 7. Na ion conductivity as a function of Sb content at 500 °C. The line is a guide for the eye, and error has been clarified in the text.

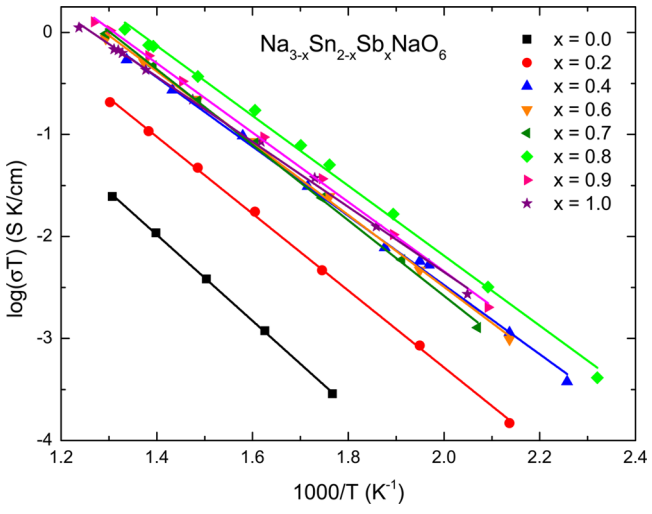

Figure 8. Na ion conductivity as a function of temperature for $Na_{3-x}Sn_{2-x}Sb_xNaO_6$, $0 \le x \le 1$. Lines are linear fits to the data.

The Na ion conductivity is facilitated by the Na vacancies created by the substitution of Sb^{5+} for Sn^{4+}. In Figure 7, the linear dependence of conductivity on Sb content, its maximum at $x = 0.8$, and its subsequent decrease are consistent with expectations for a simple system in which the ionic conductivity should go generally as the product of (f) and $(1 - f)$, where f is the fraction of occupied sites and $(1 - f)$ is the fraction of vacancies. For a triangular lattice such as the one in this study, the lowest activation energy in such a simple picture is expected for $f = 1$;[40−42] the fact that the maximum ionic conductivity is observed at $x = 0.8$ $(f = 0.73)$ suggests that correlated ion motion is present in the system. The decrease in activation energy when vacancies are initially introduced could also be indicative of a correlated conductivity mechanism. We note that it is possible for the decrease in conductivity observed for $x > 0.8$ to be due to the presence of the second polytype; however, in past work, P2 polytype materials of the $NaFeO_2$ type have been shown to have higher rather than lower conductivity compared to that of O3 polytype materials.[26,43] Thus, the 2H-like polytype is not likely to cause the decreased conductivity seen at $x > 0.8$.

The conductivity and activation energy values observed here are comparable to literature values for other Na ion conductors. Compared with E_a values of $Na_2M_2TeO_6$ (M = Ni, Co, Zn, Mg), a family of fast ion conductors with the same crystal structure, the E_a values are similar, but the highest reported conductivity is lower (0.101−0.108 S/cm at 300 °C for $Na_2Ni_2TeO_6$ versus 0.0014 S/cm at 500 °C for $Na_{2.2}Sn_{1.2}Sb_{0.8}NaO_6$).[18] The ionic conductivity of Na-deficient $Na_{3-x}Sn_{2-x}Sb_xNaO_6$ is much higher than that of α-$NaFeO_2$ (on the order of 10^{-4} S/cm at 220 °C), Na-deficient α-$Na_{0.9}FeO_2$ (on the order of 10^{-5} S/cm at 220 °C), and the Li analogue of the parent compound, Li_2SnO_3 (on the order of 10^{-8} S/cm at 300 °C).[7,8] The two canonical Na fast ion conducting compounds, β-alumina and NASICON, have lower activation energies and higher ionic conductivities than those measured here for $Na_{3-x}Sn_{2-x}Sb_xNaO_6$.[10,13] Future work on denser samples would be expected to improve the performance of these materials.

DOI: 10.1021/acs.inorgchem.5b01186
Inorg. Chem. 2015, 54, 7985−7991

4. CONCLUSIONS

We report the synthesis, structural characterization, and ionic conductivity of a new layered honeycomb oxide $Na_{3-x}Sn_{2-x}Sb_xNaO_6$, $0 \leq x \leq 1$. A new two-layer monoclinic 3R-like or O2-like structure is determined for the parent honeycomb, Na_2SnO_3. Sodium content and conductivity are tuned in this material by substitution of Sb^{5+} for Sn^{4+}, which creates vacancies in the Na layers. With low but consistent sample density values, this material has high ionic conductivity (1.43×10^{-3} S/cm at 500 °C) and is a good candidate material for further study as a solid electrolyte. Its conductivity increases linearly with Sb content (with a maximum at $x = 0.8$), showing that conductivity depends on a balance of two quantities: the mobile sodium ions available and the vacancies through which they can transport. Substituting elements with different oxidation states to control electrochemical properties such as ionic conductivity is a technique that has been particularly successful for NASICON-related materials and, as we show here, has significant potential for unstudied materials with a layered α-$NaFeO_2$ structure type.

■ ASSOCIATED CONTENT

Supporting Information

CIF file of Na_2SnO_3. The Supporting Information is available free of charge on the ACS Publications website at DOI: 10.1021/acs.inorgchem.5b01186.

■ AUTHOR INFORMATION

Corresponding Author

*E-mail: rsmaha@alumni.princeton.edu.

Present Address

[‖](R.W.S.) Department of Chemistry, Stanford University, Stanford, California 94305, United States.

Notes

The authors declare no competing financial interest.

■ ACKNOWLEDGMENTS

This research was supported by the U.S. Department of Energy, Division of Basic Energy Sciences, grant no. DE-FG02-08ER-46544. The authors thank J. Cannarella for helpful discussions.

■ REFERENCES

(1) Tarascon, J. M.; Armand, M. *Nature* **2001**, *414*, 359−67.
(2) Kundu, D.; Talaie, E.; Duffort, V.; Nazar, L. F. *Angew. Chem., Int. Ed.* **2015**, *54*, 3431−3448.
(3) Han, M. H.; Gonzalo, E.; Singh, G.; Rojo, T. *Energy Environ. Sci.* **2015**, *8*, 81−102.
(4) Mizushima, K.; Jones, P. C.; Wiseman, P. J.; Goodenough, J. B. *Mater. Res. Bull.* **1980**, *15*, 783−789.
(5) Berthelot, R.; Carlier, D.; Delmas, C. *Nat. Mater.* **2011**, *10*, 74−80.
(6) Fergus, J. W. *Solid State Ionics* **2012**, *227*, 102−112.
(7) Teo, L. P.; Buraidah, M. H.; Nor, a. F. M.; Majid, S. R. *Ionics* **2012**, *18*, 655−665.
(8) Blesa, M. C.; Moran, E.; Leon, C.; Santamaria, J.; Tornero, J. D.; Menendez, N. *Solid State Ionics* **1999**, *126*, 81−87.
(9) Palomares, V.; Serras, P.; Villaluenga, I.; Hueso, K. B.; Carretero-González, J.; Rojo, T. *Energy Environ. Sci.* **2012**, *5*, 5884−5901.
(10) Wang, J. C.; Gaffari, M.; Choi, S. *J. Chem. Phys.* **1975**, *63*, 772−778.
(11) Fuentes, R. O.; Marques, F. M. B.; Franco, J. I. *Bol. Soc. Esp. Ceram. Vidrio* **1999**, *38*, 631−634.
(12) Kohler, H.; Schulz, H. *Mater. Res. Bull.* **1985**, *20*, 1461−1471.
(13) Anantharamulu, N.; Koteswara Rao, K.; Rambabu, G.; Vijaya Kumar, B.; Radha, V.; Vithal, M. *J. Mater. Sci.* **2011**, *46*, 2821−2837.
(14) Seibel, E. M.; Roudebush, J. H.; Wu, H.; Huang, Q.; Ali, M. N.; Ji, H.; Cava, R. J. *Inorg. Chem.* **2013**, *52*, 13605−11.
(15) Dong, B.; Doi, Y.; Hinatsu, Y. *J. Alloys Compd.* **2008**, *453*, 282−287.
(16) Delmas, C.; Fouassier, C.; Hagenmuller, P. *Physica B+C* **1980**, *99*, 81−85.
(17) Paulsen, J. M.; Donaberger, R. A.; Dahn, J. R. *Chem. Mater.* **2000**, *12*, 2257−2267.
(18) Evstigneeva, M. A.; Nalbandyan, V. B.; Petrenko, A. A.; Medvedev, B. S.; Kataev, A. A. *Chem. Mater.* **2011**, *23*, 1174−1181.
(19) Smirnova, O. A.; Kharton, V. V.; Marques, F. M. B. *Bol. Soc. Esp. Ceram. Vidrio* **2004**, *43*, 679−685.
(20) Iwasaki, M.; Takizawa, H.; Uheda, K.; Endo, T. *J. Mater. Chem.* **2002**, *12*, 1068−1070.
(21) Hubbert-Paletta, E.; Hoppe, R.; Kreuzburg, G. *Z. Anorg. Allg. Chem.* **1971**, *379*, 255−261.
(22) Rodriguez-Carvajal, J. *Phys. B* **1993**, *192*, 55−69.
(23) Momma, K.; Izumi, F. *J. Appl. Crystallogr.* **2011**, *44*, 1272−1276.
(24) Singh, Y.; Gegenwart, P. *Phys. Rev. B: Condens. Matter Mater. Phys.* **2010**, *82*, 064412.
(25) Krizan, J.; Roudebush, J. H.; Fox, G. M.; Cava, R. J. *Mater. Res. Bull.* **2014**, *52*, 162−166.
(26) Politaev, V. V.; Nalbandyan, V. B.; Petrenko, A. A.; Shukaev, I. L.; Volotchaev, A. L.; Medvedev, B. S. *J. Solid State Chem.* **2010**, *183*, 684−691.
(27) Choi, S. K.; Coldea, R.; Kolmogorov, A. N.; Lancaster, T.; Mazin, I. I.; Blundell, S. J.; Radaelli, P. G.; Singh, Y.; Gegenwart, P.; Choi, K. R.; Cheong, S.-W.; Baker, P. J.; Stock, C.; Taylor, J. *Phys. Rev. Lett.* **2012**, *108*, 127204.
(28) Roudebush, J. H.; Andersen, N. H.; Ramlau, R.; Garlea, V. O.; Toft-Petersen, R.; Norby, P.; Schneider, R.; Hay, J. N.; Cava, R. J. *Inorg. Chem.* **2013**, *52*, 6083−6095.
(29) Warren, B. E. *Phys. Rev.* **1941**, *59*, 693−698.
(30) Seibel, E. M.; Roudebush, J. R.; Ali, M. N.; Ross, K. A.; Cava, R. J. *Inorg. Chem.* **2014**, *53*, 10989−10995.
(31) Roudebush, J. R.; Sahasrabudhe, G.; Bergman, S. L.; Cava, R. J. *Inorg. Chem.* **2015**, *54*, 3203−3210.
(32) Miura, Y.; Hirai, R.; Kobayashi, Y.; Sato, M. *J. Phys. Soc. Jpn.* **2006**, *75*, 084707.
(33) Schmidt, W.; Berthelot, R.; Sleight, A. W.; Subramanian, M. A. *J. Solid State Chem.* **2013**, *201*, 178−185.
(34) Viciu, L.; Huang, Q.; Morosan, E.; Zandbergen, H. W.; Greenbaum, N. I.; McQueen, T.; Cava, R. J. *J. Solid State Chem.* **2007**, *180*, 1060−1067.
(35) Viciu, L.; Bos, J. W. G.; Zandbergen, H. W.; Huang, Q.; Foo, M. L.; Ishiwata, S.; Ramirez, A. P.; Lee, M.; Ong, N. P.; Cava, R. J. *Phys. Rev. B: Condens. Matter Mater. Phys.* **2006**, *73*, 174104.
(36) Amatucci, G. G.; Tarascon, J. M.; Klein, L. C. *J. Electrochem. Soc.* **1996**, *143*, 1114−1123.
(37) Berthelot, R.; Schmidt, W.; Muir, S.; Eilertsen, J.; Etienne, L.; Sleight, A. W.; Subramanian, M. A. *Inorg. Chem.* **2012**, *51*, 5377−5385.
(38) Roudebush, J. H.; Cava, R. J. *J. Solid State Chem.* **2013**, *204*, 178−185.
(39) Montes, J. M.; Cuevas, F. G.; Cintas, J. *Appl. Phys. A: Mater. Sci. Process.* **2008**, *92*, 375−380.
(40) van der Ven, A.; Ceder, G. *Electrochem. Solid-State Lett.* **1999**, *3*, 301−304.
(41) van der Ven, A.; Ceder, G. *J. Power Sources* **2001**, *97−98*, 529−531.
(42) van der Ven, A.; Ceder, G. *Phys. Rev. B: Condens. Matter Mater. Phys.* **2001**, *64*, 184307.
(43) Mo, Y.; Ong, S. P.; Ceder, G. *Chem. Mater.* **2014**, *26*, 5208−5214.

DOI: 10.1021/acs.inorgchem.5b01186
Inorg. Chem. 2015, 54, 7985−7991